On the Effect of Boron Modifications of Palladium Catalysts for the Production of Hydrogen from Formic Acid

ARTICLE *in* ACS CATALYSIS · SEPTEMBER 2015

Impact Factor: 9.31 · DOI: 10.1021/acscatal.5b01497

4 AUTHORS, INCLUDING:

Jong Suk Yoo

Stanford University

7 PUBLICATIONS **36** CITATIONS

SEE PROFILE

Zhijian Zhao

Tianjin University

23 PUBLICATIONS **216** CITATIONS

SEE PROFILE

Felix Studt

Stanford University

93 PUBLICATIONS **2,631** CITATIONS

SEE PROFILE

ACS Catalysis

Research Article

pubs.acs.org/acscatalysis

Effect of Boron Modifications of Palladium Catalysts for the Production of Hydrogen from Formic Acid

Jong Suk Yoo,[†,‡] Zhi-Jian Zhao,[†,‡] Jens K. Nørskov,[†,‡] and Felix Studt*[,†,‡]

[†]SUNCAT Center for Interface Science and Catalysis, SLAC National Accelerator Laboratory, 2575 Sand Hill Road, Menlo Park, California 94025, United States

[‡]Department of Chemical Engineering, Stanford University, Stanford, California 94305, United States

Supporting Information

ABSTRACT: In this study, we explore the effect of light nonmetal dopants (e.g., boron, carbon, and nitrogen) on the catalytic properties of transition-metal surfaces using the recently discovered boron-doped palladium catalyst for formic acid decomposition as an example. We use periodic density functional theory (DFT) calculations to derive an understanding of how subsurface boron modifies the palladium catalyst to be more active, and we find that the effect of the boron modification of palladium is different depending on the class of an adsorbate. Our DFT calculation results are also coupled to the microkinetic model of formic acid decomposition published previously to show that the catalytic properties of boron-doped palladium can be analyzed within the same conceptual framework used for understanding the catalytic trends of (undoped) transition-metal and alloy catalysts.

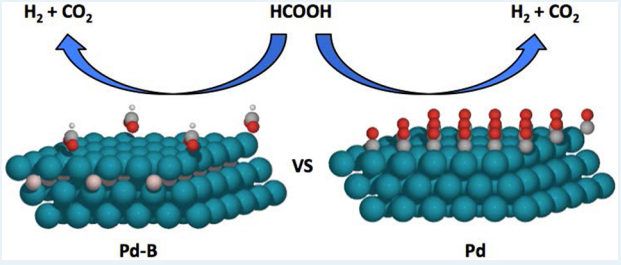

KEYWORDS: *formic acid, palladium, boron, hydrogen, density functional theory, microkinetics*

INTRODUCTION

Transition-metal catalysts form one of the backbones of the chemical industry,[1] and it is clear that the search for renewable energy solutions will heavily depend upon their employments. The performance of a transition-metal catalyst is often boosted via the addition of a promoter[2−4] or by alloying with another element.[5−9] The promoter (or the second element of an alloy) often accounts for a minor part of the catalytic system, only slightly modifying the energetics of the reaction intermediates via shifting of the d-band center[10,11] or electrostatic interactions.[5] Another means of altering the catalytic properties of transition-metal surfaces is achieved via the incorporation of relatively small atoms, such as hydrogen,[12−14] boron,[15−20] and carbon,[21] into lattices of the metals. For example, Pd has been shown to exhibit increased catalytic selectivity for acetylene hydrogenation upon incorporation of carbon into its subsurface.[21] The boron doping of Co catalysts for the Fischer−Tropsch synthesis has also been shown to suppress the deactivation of the catalysts efficiently.[18] Recently, a boron-doped Pd catalyst has been shown to produce H_2 from formic acid at a high rate,[19] a finding that is valuable for H_2 storage solutions.

Formic acid, having gravimetric and volumetric H_2 capacities of 4.4 wt % and 53.4 g/L, respectively, can become a suitable H_2 storage material if we can find catalysts that can selectively decompose formic acid to H_2 and CO_2 (instead of H_2O and CO) under mild conditions.[22,23] Previously, we have used density functional theory (DFT) calculations coupled with the development of scaling relations[24,25] and a microkinetic model in order to identify what is needed for a catalyst material to be extremely active and selective for formic acid dehydrogenation.[26] This study led to the so-called volcano plots where the catalytic activities and selectivities of transition-metal surfaces are mapped out as functions of two independent descriptors, the CO* and OH* binding energies.

In this study, we present a theoretical insight into how subsurface boron modifies the Pd surface to gear it toward an active and selective catalyst for formic acid dehydrogenation at room temperatures. In addition, the previously developed descriptor-based model[26] is used to show that the effect created by the subsurface doping can be understood within the same conceptual framework used for understanding the catalytic trends of (undoped) transition-metal surfaces. The theoretical insight presented in this study should help understand and develop the field of subsurface modifications of transition-metal catalysts with light nonmetal elements such as boron, carbon, and nitrogen.

RESULTS AND DISCUSSION

First, we start by calculating boron adsorption energies (relative to gas-phase B_2H_6) on different surface sites of Pd(111) and Pd(211) for various boron coverages (see Figure 1). Among different surface sites of the (111) facet, boron adsorbs the most strongly on the HCP site (see Table S1 of Supporting

Received: July 16, 2015
Revised: September 23, 2015
Published: September 28, 2015

DOI: 10.1021/acscatal.5b01497
ACS Catal. 2015, 5, 6579−6586

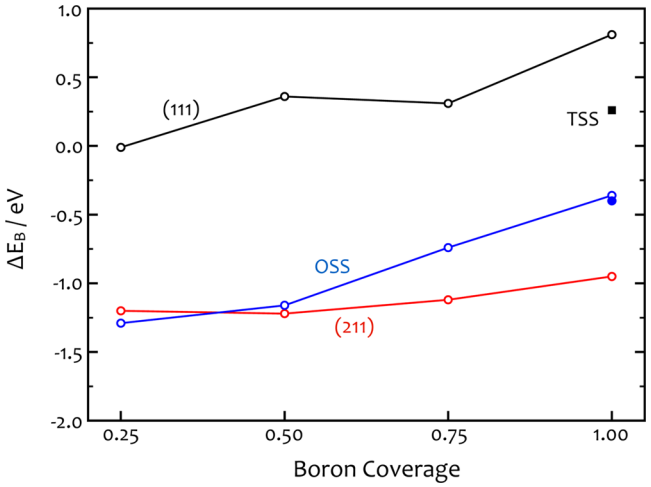

Figure 1. Average adsorption energies of boron (at 0 K) at different sites of the palladium surface and subsurface (black circles: adsorption on Pd(111); red circle: adsorption on the 4-fold site of Pd(211); blue circle: adsorption in the octahedral subsurface site of Pd(111); black square: adsorption in the tetrahedral subsurface site of Pd(111)). The full blue circle shows the average boron adsorption energy calculated on the reconstructed surface that was obtained with a (4 × 4 × 5) supercell at the boron coverage of 1 ML. No significant reconstructions of the Pd(111) surfaces are found for the boron coverage of 0.50 or 0.75 ML (see Figure S7 of SI for details). The average adsorption energies of boron shown here are with respect to the decomposition of gas-phase B_2H_6 to adsorbed boron and gas-phase H_2.

Information (SI) for adsorption energies of boron on other surface sites of Pd(111) and Figure S1 of SI for pictures of the adsorption sites). However, boron adsorption on this site is only thermo-neutral (0.0 eV) at 0.25 ML of boron and becomes endothermic (0.8 eV) when the boron coverage increases to 1 ML. On the other hand, boron adsorptions on the surface sites of (211) facet are found to be much stronger (exothermic) where boron is the most stable on the 4-fold site (see Table S1 of SI for adsorption energies of boron on other surface sites of Pd(211) and Figure S1 of SI for pictures of the adsorption sites). Boron adsorption on this site is exothermic (−1.20 eV) at 0.25 ML of boron and becomes slightly less exothermic (−0.95 eV) when the boron coverage increases to 1 ML.

Next, boron adsorptions in the octahedral and tetrahedral subsurface sites of Pd(111) are considered (boron adsorptions in the subsurface sites of Pd(211) are not considered as they are found to be less favorable than that on the 4-fold site of Pd(211) for most boron coverages, see Table S1 of SI). The octahedral subsurface site (OSS) is located beneath the 3-fold FCC site, whereas the tetrahedral subsurface site (TSS) is located beneath the 3-fold HCP site (see Figure S1 of SI). The boron atoms in TSS are much less stable than those in OSS. In fact, the TSS boron atoms all relaxed to OSS during geometry optimization for the boron coverage of 0.25, 0.50, and 0.75 ML. Figure 1 shows that at 0.25 ML of boron, boron is slightly more stable when it is in OSS of the (111) facet than on the 4-fold site of the (211) facet. However, this preference changes as the average adsorption energy of boron in OSS of the (111) facet weakens significantly, although that on the 4-fold site of the (211) facet weakens slightly with increasing boron coverage.

The adsorption preference for a subsurface site in Pd(111) and that for a surface site on Pd(211), as well as the weakening of the adsorption energy with increasing dopant coverage, have all been previously observed for carbon-modified Pd systems as well.[27] Compared to subsurface boron in Pd, however, subsurface carbon in Pd is found to be much less stable when taken relative to the most stable gas-phase species, that is, B_2H_6 for boron and CH_4 for carbon (see Table S1 and Figure S2 of SI for adsorption energies of carbon on Pd). Thus, only very high carbon chemical potentials (more than 1.4 eV relative to gas-phase methane; as can be achieved with high concentrations of acetylene)[21,27] will lead to an appreciable coverage of subsurface carbon in Pd. The same is also true for subsurface nitrogen in Pd, which is found to be quite unstable (by more than 1.5 eV) when compared to gas-phase NH_3 (see Table S1 and Figure S2 of SI for adsorption energies of nitrogen on Pd).

Finally, we have considered the tendency of subsurface boron (as well as subsurface carbon and nitrogen) to migrate into bulk Pd. The OSS boron atom in the second subsurface layer of Pd(111) is found to be 0.15 eV less stable than that in the first subsurface layer, and the boron atom in bulk palladium boride (Pd_4B) is found to be considerably less stable (i.e., by 1.25 eV) relative to that in the first subsurface layer of Pd(111). To conclude, because boron is found to be the most stable on the 4-fold site of the (211) facet, this site would be first completely covered by boron. The next most stable adsorption site (i.e., OSS of the (111) facet) will then be occupied by additional boron. The OSS boron atoms have strong interactions between them, leading to a significant weakening of their binding energies with increasing coverage of OSS boron.

Figure 2 shows the effect of OSS boron on chemisorption energies of all the reaction species involved in formic acid decomposition. It can be seen that the chemisorption energies are quite strongly dependent on the coverage of OSS boron. More interestingly, the effect seems to be opposite for the carbon-bound (COOH* and CO*) and oxygen-bound (HCOO* and OH*) species. The chemisorption energies of COOH* and CO* weaken with increasing coverage of OSS boron, ultimately leading to significant energy differences of 0.58 and 0.74 eV, respectively, when those on Pd(111) are compared to those on Pd(111) containing 1 ML of OSS boron (this surface will now be denoted as $Pd(B/OSS)^{1\ ML}$). This effect of OSS boron on chemisorption energies of carbon-bound species is quite similar to what has been previously observed for some carbon-modified Pd catalysts.[27] On the other hand, the chemisorption energies of HCOO* and OH* strengthen with increasing coverage of OSS boron, ultimately leading to significant energy differences of 0.50 and 0.34 eV, respectively, when the OSS boron coverage increases from 0 to 1 ML. The binding characteristics of H* has been studied to be quite similar to those of carbon-bound species,[26] and thus, its chemisorption energy also weakens from −0.29 eV (on Pd(111)) to +0.10 eV (on $Pd(B/OSS)^{1\ ML}$). Finally, we note here that subsurface carbon and nitrogen in Pd have similar effects as subsurface boron in Pd (see Figure S3 of SI).

The different trends in chemisorption energies of the carbon-bound and oxygen-bound adsorbates can be explained through a detailed analysis of the structures of the boron-modified Pd surfaces, as they seem to vary considerably depending on the class of an adsorbate. For example, Figure 3 shows Pd(B/OSS) surfaces at different coverages of OSS boron ($\theta^{B/OSS}$) slightly reconstructed upon CO* and OH* adsorption. In the case of CO* adsorption, when $\theta^{B/OSS} \geq 0.75$, OSS boron atoms assemble to form a triangular structure beneath a Pd atom,

DOI: 10.1021/acscatal.5b01497
ACS Catal. 2015, 5, 6579−6586

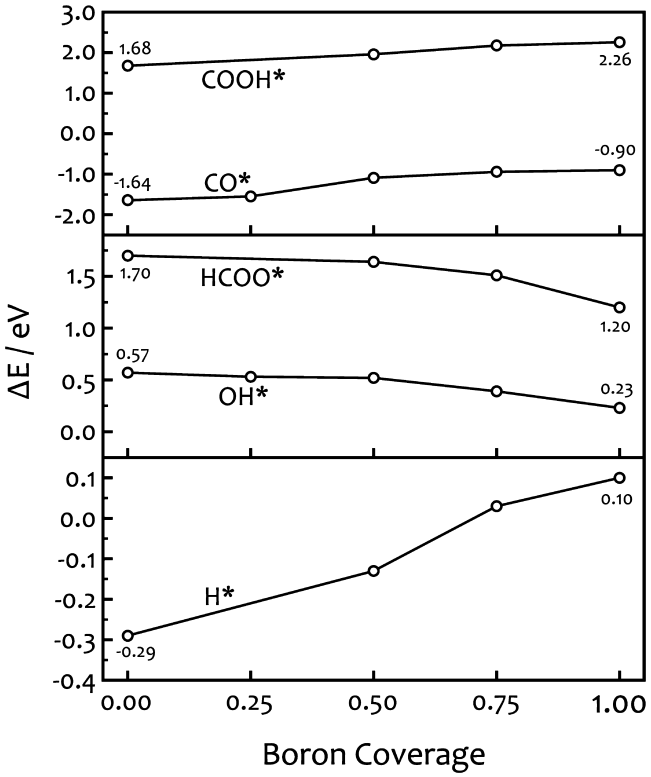

Figure 2. Average chemisorption energies of COOH*, CO*, HCOO*, OH*, and H* on Pd(111) as a function of the OSS boron coverage. The energies of COOH*, HCOO*, OH*, and H* are relative to gas-phase CH_4, H_2O, and H_2 whereas those of CO* are taken relative to gas-phase CO.

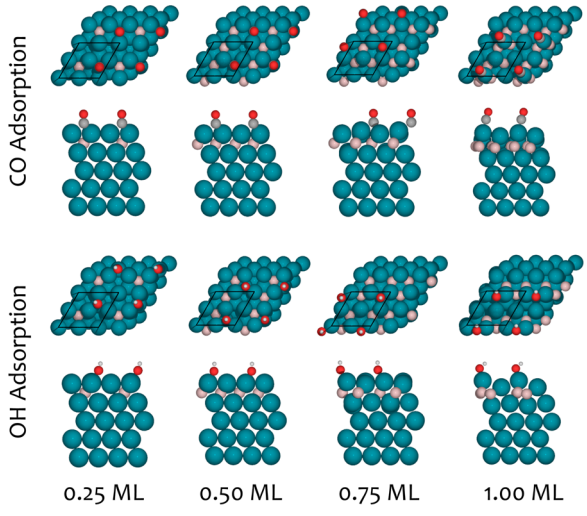

Figure 3. Top and side views of the structures of the subsurface-boron modified Pd(111) surfaces upon adsorption of either CO* or OH* for the boron coverages of 0.25, 0.5, 0.75, and 1 ML. Palladium is shown in turquoise, boron in pink, carbon in gray, oxygen in red, and hydrogen in white. The black rectangle depicts the size of the unit cell in all calculations.

lifting the Pd atom relative to the surface plane. On the other hand, in the case of OH* adsorption, when $\theta^{B/OSS} = 1.00$, OSS boron atoms orient to form a zigzag structure beneath a row of Pd atoms, lifting the entire Pd row relative to the surface plane. As a result, a step-like surface is created upon adsorption of OH* on $Pd(B/OSS)^{1\ ML}$, which allows forming a stronger bond between OH* and the Pd surface. Similar arguments can be made for all carbon-bound versus oxygen-bound species involved in formic acid decomposition (see Figure S4 of SI).

We will now examine how the reaction energetics of formic acid decomposition change upon the subsurface modification of Pd(111) with boron. Figures 4a–c show the three different formic acid decomposition pathways that have been established in earlier theoretical studies.[26,28] Formic acid decomposes via either the formate (HCOO*) or carboxyl (COOH*) intermediate. Although the former pathway only produces CO_2 and H_2 (see Figure 4a), the latter pathway produces both $CO_2 + H_2$ (see Figure 4b) and $CO + H_2O$ (see Figure 4c). We

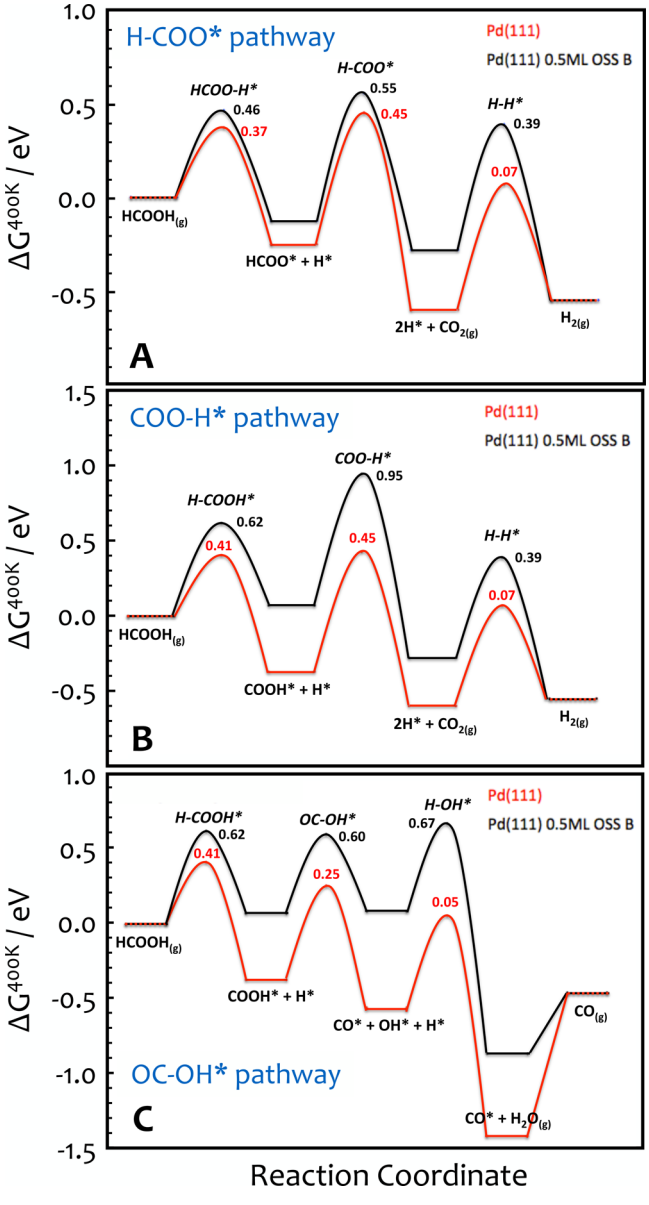

Figure 4. Free-energy diagrams for formic acid decomposition via the (a) H–COO*, (b) COO-H*, and (c) OC–OH* pathways over Pd(111) and $Pd(B/OSS)^{0.5\ ML}$ at 400 K and 1 bar of all gas-phase molecules. Only the minimum energy pathways are shown in the diagrams. The most stable adsorption configuration for HCOO* is bidentate on Pd(111) and monodentate on $Pd(B/OSS)^{0.5\ ML}$. However, the barrier for $H–COO*_{bidentate}$ is found to be lower than that for $H–COO*_{monodentate}$ on both surfaces. All free energies are shown relative to gas-phase formic acid.

DOI: 10.1021/acscatal.5b01497
ACS Catal. 2015, 5, 6579–6586

will now compare the reaction energetics of the three different pathways on Pd(111) with those on Pd(111) containing an intermediate OSS boron coverage of 0.5 ML (i.e., Pd(B/OSS)$^{0.5\ ML}$) to investigate the effect of the subsurface-boron modification of Pd(111) in detail.

As can be seen in Figure 4 (see Table S2 of SI for values), the transition-state energies are generally higher on Pd(B/OSS)$^{0.5\ ML}$ than on Pd(111). They are particularly higher (by 0.2−0.5 eV) for the transition states that bind to the surface through both carbon and hydrogen (e.g., H−COOH* and COO-H*). This is due to the weakening of the adsorption of both carbon- and hydrogen-bound species upon introduction of subsurface boron (see Figure 2). For the transition states that bind to the surface through both oxygen and hydrogen (e.g., HCOO-H* and H−COO*), the transition-state energy differences between Pd(111) and Pd(B/OSS)$^{0.5\ ML}$ are only about 0.1 eV. Here, a trade off between the two opposite effects of subsurface boron (i.e., strengthening of the oxygen-bound adsorptions and weakening of the hydrogen-bound adsorptions) is reflected to result in an almost unchanged transition-state energy. All energy barriers on Pd(111) and Pd(B/OSS)$^{0.5\ ML}$ are still rather low (below 1 eV in free energy) rendering both surfaces high catalytic activities. However, catalytic activity depends not only on the free-energy barriers but also on the free-energy wells created by strongly binding reaction species, such as CO*, COOH*, and HCOO*, as the presence of these species would decrease the amount of the active sites available on the catalyst surface. Figure 4 shows that the free-energy wells created by these species are shallower on Pd(B/OSS)$^{0.5\ ML}$ than on Pd(111), indicating that the former surface can be more active than the latter depending on the reaction condition. However, quantitatively analyzing the effect of subsurface boron on the reaction rates from simply the free energy diagrams is rather difficult. Kinetic models are needed in order to properly evaluate how catalytic activity changes upon boron doping.

Let us now discuss the kinetics of formic acid decomposition obtained from the reaction energetics shown in Figure 4 using a microkinetic model. The microkinetic model used here is identical to the one reported in our earlier work where it is described in detail (also see SI).[26] Figure 5a,b show the calculated turnover frequencies for formic acid dehydrogenation and dehydration on Pd(111) and Pd(B/OSS)$^{0.5\ ML}$ as a function of temperature at two different CO partial pressures (p_{CO} = 1 and 100 ppm). The formic acid dehydrogenation rate is found to be orders of magnitude faster than the formic acid dehydration rate on both surfaces, particularly at low temperatures, indicating selective production of H_2. Under severe CO-poisoning conditions (low T and/or high p_{CO}), however, the catalytic activities of Pd(B/OSS)$^{0.5\ ML}$ are much higher than those of Pd(111). On the other hand, under mild CO-poisoning conditions (high T and/or low p_{CO}), the catalytic activities of Pd(B/OSS)$^{0.5\ ML}$ are either comparable to or slightly higher than those of Pd(111). Figure 5c also shows that CO production is suppressed more on Pd(B/OSS)$^{0.5\ ML}$ than on Pd(111) (see the red curves (p_{CO} = 1 ppm)). These microkinetic results are in agreement with previous experimental studies that found an enhancement in the formic acid dehydrogenation rate by a factor of 3 upon doping of boron to the Pd catalyst.[19] The reported experimental rates for the production of H_2 from formic acid are also shown in Figure 5a for both Pd and boron-doped Pd

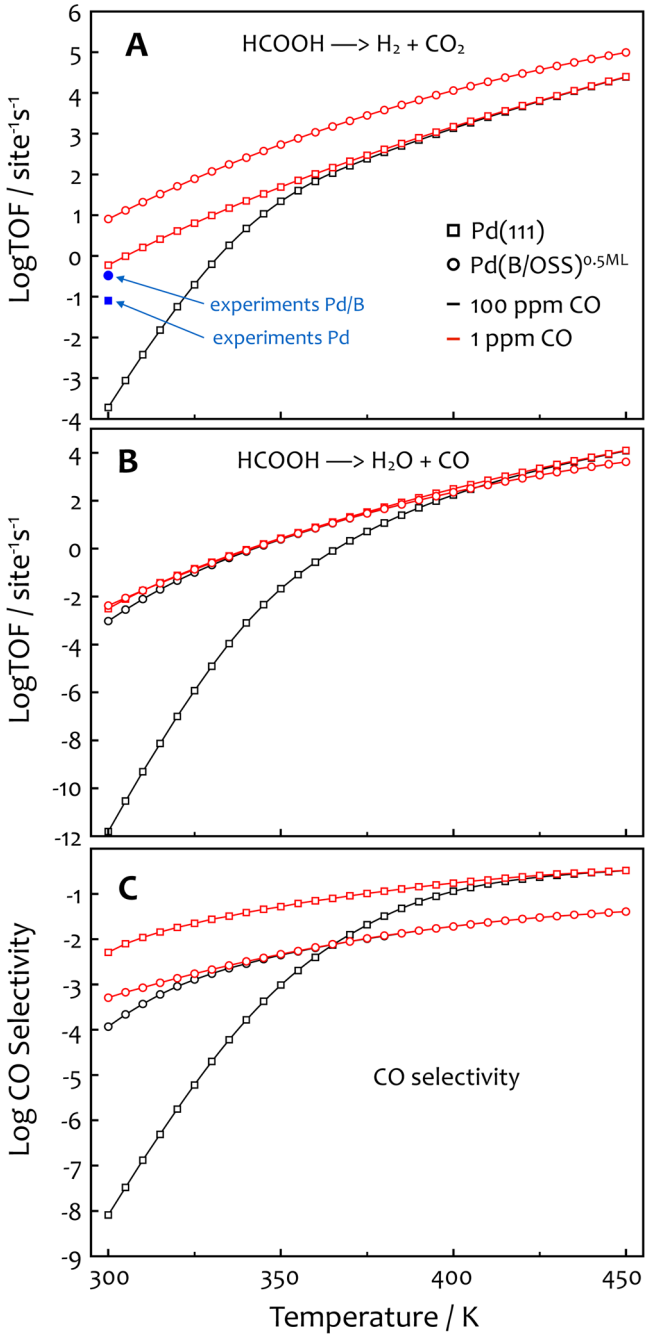

Figure 5. Turnover frequencies (TOF) for formic acid (a) dehydrogenation, and (b) dehydration on Pd(111) (square) and Pd(B/OSS)$^{0.5\ ML}$ (circle). The reaction conditions used are p_{HCOOH} = 0.97, p_{CO_2} = 0.01, p_{H_2} = 0.01, p_{H_2O} = 0.01 bar. The TOF are shown for both low (p_{CO} = 1 ppm (red)) and high (p_{CO} = 100 ppm (black)) partial pressures of CO. (c) CO selectivities of Pd(111) (square) and Pd(B/OSS)$^{0.5\ ML}$ (circle). Note that the TOF for formic acid dehydrogenation on Pd(B/OSS)$^{0.5\ ML}$ at p_{CO} = 100 ppm (black circles in (a)) are calculated to be essentially the same as those at p_{CO} = 1 ppm (red circles in (a)), hence both curves are on top of each other.

(Pd/B). Thus, we can conclude here that the effect of having subsurface boron in Pd is to enhance the CO* tolerance of Pd.

A question still remains as to why clean Pd(111) is not any better than Pd(B/OSS)$^{0.5\ ML}$ under mild CO-poisoning conditions (high T and/or low p_{CO}), although the free-energy

DOI: 10.1021/acscatal.5b01497
ACS Catal. 2015, 5, 6579−6586

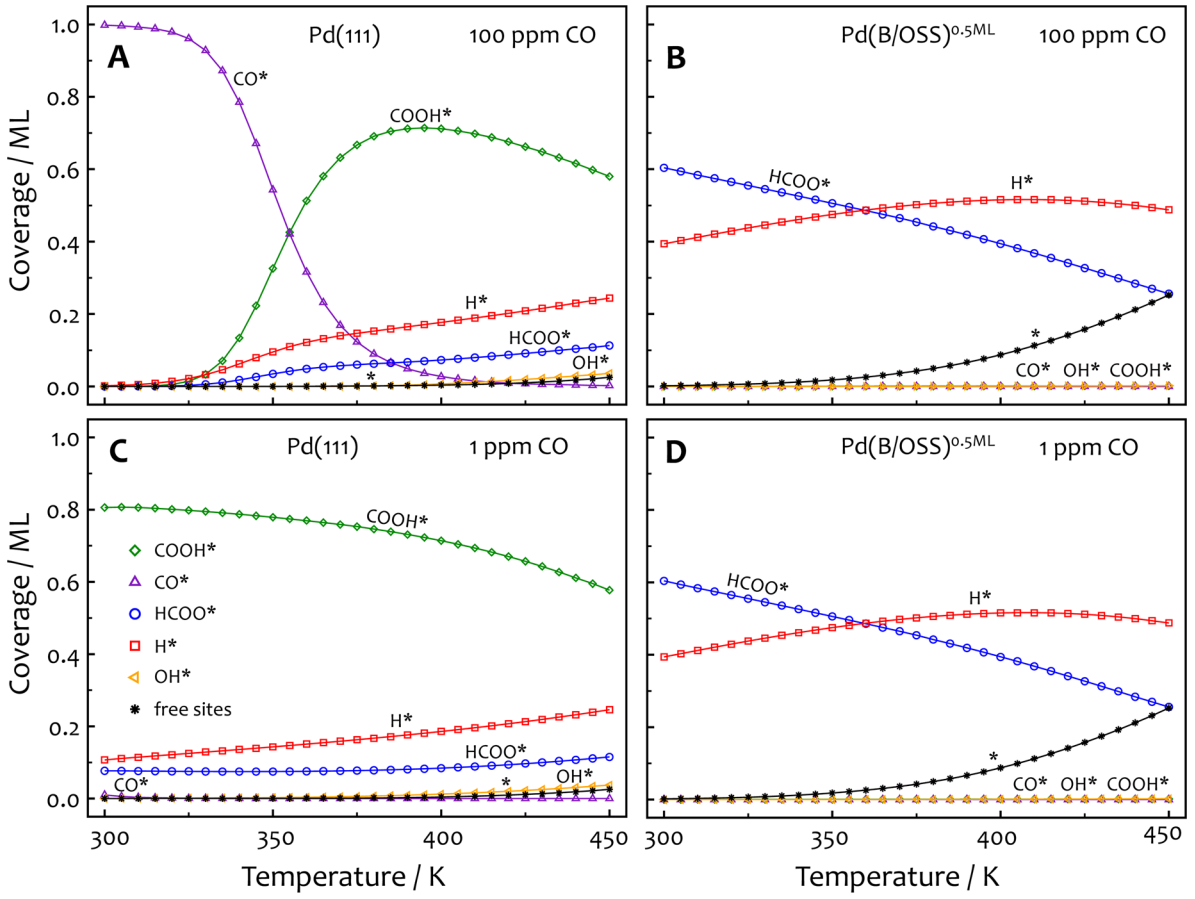

Figure 6. Steady-state coverages of all the reaction intermediates adsorbed on Pd(111) at (a) p_{CO} = 100 ppm, and (c) p_{CO} = 1 ppm, and on Pd(B/OSS)$^{0.5\ ML}$ at (b) p_{CO} = 100 ppm and (d) p_{CO} = 1 ppm, plotted as a function of temperature as obtained from the microkinetic model. All other pressures are kept constant at (p_{HCOOH} = 0.97, p_{CO_2} = 0.01, p_{H_2} = 0.01, and p_{H2O} = 0.01 bar).

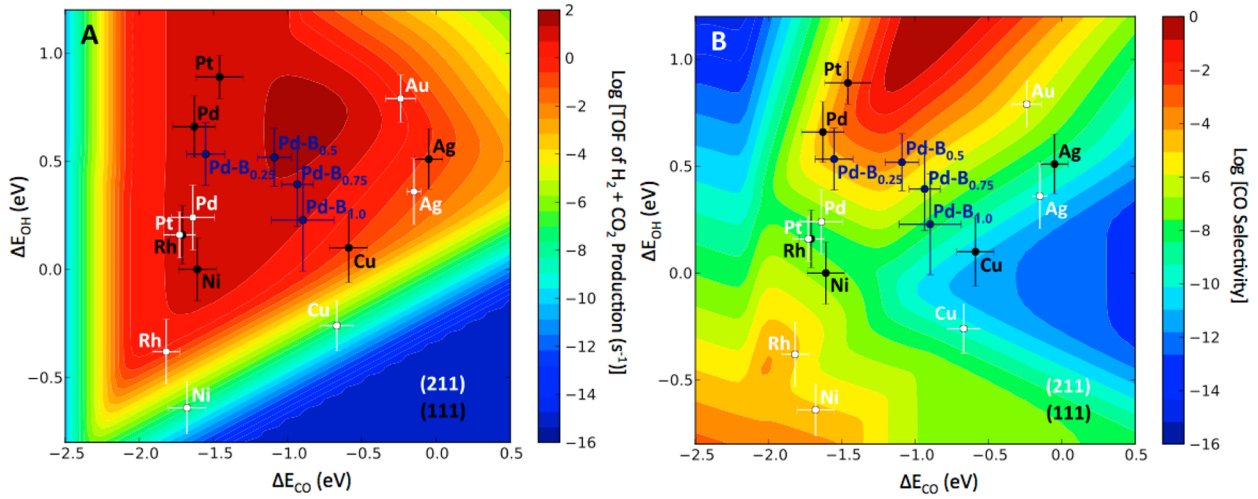

Figure 7. (a) Theoretical activity volcano for the production of H_2 (and CO_2) from formic acid and (b) the calculated CO (and H_2O) selectivities. The logarithms of both quantities are plotted as functions of ΔE_{CO} and ΔE_{OH} that were taken relative to electronic energies of CO, H_2, and H_2O in the gas-phase. The CO selectivity is defined as the production rate of CO + H_2O divided by the total rate of formic acid decomposition. The calculated ΔE_{CO} and ΔE_{OH} for various fcc(211), fcc(111), and the boron-modified Pd(111) surfaces are depicted in white, black, and blue, respectively. The reaction conditions used are p_{HCOOH} = 0.97 bar, p_{CO_2} = 0.01 bar, p_{H_2} = 0.01 bar, p_{H_2O} = 0.01 bar, p_{CO} = 100 ppm, and T = 400 K). These volcano plots are identical to what has been reported earlier.[26] The error bars are obtained using the BEEF-vdW ensemble of exchange–correlation functionals.[36]

barriers are found to be generally lower on the former surface than the latter (see Figure 4). This question can be addressed when the coverages of the reaction species at steady state are compared (see Figure 6). Under mild CO-poisoning conditions (high T and/or low p_{CO}), for example, COOH* dominates the Pd(111) surface whereas HCOO* and H* dominate the Pd(B/

DOI: 10.1021/acscatal.5b01497
ACS Catal. 2015, 5, 6579–6586

OSS)$^{0.5\ ML}$ surface. Figure S5 of SI shows the contribution of the H−COO* pathway to the production of H_2 from formic acid on the two surfaces. It can be seen that 60−82% of H_2 is produced via HCOO* on Pd(111), indicating that COOH* is more of a spectator species blocking the active site rather than a reaction species being directly consumed to produce H_2. On the other hand, nearly 100% of H_2 is produced via HCOO* on Pd(B/OSS)$^{0.5\ ML}$, indicating that HCOO* and H* are the reaction species being directly consumed to produce H_2 rather than poisons. Hence, having a lot of COOH* on Pd(111) is detrimental to the formic acid dehydrogenation rate, whereas having a lot of HCOO* and H* on Pd(B/OSS)$^{0.5\ ML}$ is not that critical. To conclude, Pd(B/OSS)$^{0.5\ ML}$ is a better catalyst than Pd(111) due to improved CO* tolerance under severe CO-poisoning conditions, but it is also better due to improved COOH* tolerance under mild CO-poisoning conditions.

However, note that all the microkinetic results shown here (e.g., Figure 5 and 6) are based on the reaction energetics obtained at the fixed adsorbate coverage of 0.25 ML. Therefore, we have investigated the effect of the adsorbate−adsorbate interactions by calculating the adsorption energies of H*, CO*, HCOO*, and COOH* at different coverages (see Table S4 and S5 of SI). The adsorbate−adsorbate interactions are found to be negligible for H* and rather small for HCOO* and COOH*. Even for the latter species, the interactions are present only at extremely high coverages (larger than 0.7 ML). On the other hand, the adsorbate−adsorbate interactions are found to be quite significant for CO* as also reported previously.[29,30] However, our microkinetic analysis does not show any significant coverages of CO* on Pd(B/OSS)$^{0.5\ ML}$ (see Figure 6b,d), hence validating the (low-coverage) approach taken here. The clean Pd(111) surface is shown to have extremely high coverages of CO (∼1 ML) at temperatures lower than 350 K (see Figure 6a,c). In this temperature region, we expect deviations from our kinetic results if the adsorbate−adsorbate interactions were included in the microkinetic model. However, because the CO coverage on Pd(111) is found to be lower than 0.4 ML for temperatures higher than 350 K, we do not expect any significant effect of the adsorbate−adsorbate interactions under the reaction condition employed (note that Figure 4 and 7 are obtained at 400 K).

Previously, we have established theoretical activity and selectivity volcanoes for formic acid decomposition on transition-metal surfaces using the adsorption energies of CO* (ΔE_{CO}) and OH* (ΔE_{OH}) as descriptors.[26] We find that the same descriptors can be used to locate the various boron-doped Pd surfaces on the volcano plots, as we discover that adsorption energies of the reaction intermediates and transition states on Pd(B/OSS)$^{0.5\ ML}$ generally follow the scaling relations obtained based on transition-metal surfaces (see Figure S6 of SI). The locations of the various boron-doped Pd surfaces on the activity and selectivity volcanoes are shown in Figure 7a,b, respectively (note that Figure 7b shows CO selectivities instead of H_2 selectivities). It can be seen that the boron modification of Pd moves the Pd(111) surface to the most active, yet quite H_2 selective region of the volcanoes. So far only the Ag[31−33] or Au[34,35] modified Pd surfaces have been identified to be in this region.[26] In fact, Pd(B/OSS)$^{0.5\ ML}$ is very close to Ag_3Pd (the most active material found to date) in the descriptor space with $\Delta\Delta E_{CO}$ = 0.06 eV and $\Delta\Delta E_{OH}$ = 0.05 eV.

CONCLUSIONS

Theoretical methods have been taken to study the reaction energetics and kinetics of formic acid decomposition on boron-doped Pd. We have shown that boron adsorption in the octahedral subsurface site of Pd(111) is highly favorable, and that this subsurface-boron modification of Pd has different effects on the chemisorption energies of different adsorbates; that is, the chemisorption energies of the carbon-bound species weaken, whereas those of the oxygen-bound species strengthen with increasing subsurface-boron coverage. The increased rate of formic acid decomposition on boron-doped Pd has then been explained by the destabilization of CO* and COOH* on the catalyst surface. Relatively low coverages of these poisoning species on boron-doped Pd leave more free sites on the catalyst surface where formic acid can be dehydrogenated via the HCOO* intermediate. Finally, we have shown that adsorption energies of all the reaction intermediates and transition states on boron-doped Pd generally follow the trends of those on clean transition-metal surfaces. Accordingly, the descriptor-based analysis has been used to find that Pd(111) containing half a monolayer of subsurface boron in the octahedral subsurface site is indeed one of the most active formic acid decomposition catalysts, a finding that is in good agreement with experimental observations.

COMPUTATIONAL DETAILS

Periodic DFT calculations were carried out using the Atomic Simulation Environment (ASE)[37] in connection with the Quantum ESPRESSO code.[38] We employed the BEEF-vdW functional[39] that has been shown to describe chemisorption as well as physisorption energies on transition-metal surfaces quite accurately.[40] In particular, this functional has proven to yield a quantitative description of CO_2 hydrogenation to methanol over copper surfaces[41,42] involving many of the species occurring in the present study. A kinetic energy cutoff of 500 eV and a density energy cutoff of 5000 eV have been used for all calculations. The ionic cores were described by Vanderbilt ultrasoft pseudopotentials.[43] The slab models, which were consistent with five atomic layers, separated by more than 13 Å of vacuum space in the direction perpendicular to the surface plane, were created by infinitely repeating a (2 × 2 × 5) supercell for a Pd(111) surface, and a (1 × 4 × 5) supercell for a Pd(211) surface. In the slab models, the top three atomic layers (including the adsorbate) were allowed to relax, whereas the bottom two layers were fixed at their bulk positions. The Brillouin zones were sampled using either (4 × 4 × 1) or (8 × 2 × 1) Monkhorst−Pack k-point mesh[44] for the (2 × 2 × 5) or (1 × 4 × 5) supercell, respectively. The climbing image nudged elastic band method was used to identify the transition-states.[45] The convergence criterion for optimization was a maximum force of 0.05 eV/Å per atom. The free-energy corrections for the adsorbed species were obtained from the vibrational frequencies in the harmonic approximation. Gas-phase corrections[46] were employed for CO_2 (0.41 eV), HCOOH (0.41 eV), and H_2 (0.09 eV) as described elsewhere.[42] The uncertainty of DFT energies is obtained through an ensemble of exchange−correlation functionals representing the known computational errors of the BEEF-vdW functional as reported elsewhere.[36] The microkinetic model used here is the same as the one reported previously,[26] and more details can be found in SI. Finally, we note here that we have checked for both the boron-mediated and CO*/HCOO*-mediated reconstructions

DOI: 10.1021/acscatal.5b01497
ACS Catal. 2015, 5, 6579−6586

of the boron-doped Pd(111) surfaces using a global optimization method that implements genetic algorithms.[47−49] (4 × 4 × 5) supercells were used for all these calculations (see SI for more details of the global optimization method). We find that the calculation results obtained using (2 × 2 × 5) supercells are quite similar to those obtained using larger supercells for all boron-doped Pd(111) surfaces, except the one with 1 ML of boron (see Figure S7, S8 and Table S3, S4, S5 of SI). In the case of the (4 × 4 × 5) supercell calculation, 1 ML of boron induced a significant reconstruction of the Pd(111) surface. This reconstructed surface was 0.04 eV/boron more stable than the unreconstructed surface found with a (2 × 2 × 5) supercell.

■ ASSOCIATED CONTENT

Supporting Information

The Supporting Information is available free of charge on the ACS Publications website at DOI: 10.1021/acscatal.5b01497.

Details of the microkinetic model, tables and figures showing additional data, and details of the global optimization method (PDF)

■ AUTHOR INFORMATION

Corresponding Author

*E-mail: studt@slac.stanford.edu.

Notes

The authors declare no competing financial interest.

■ ACKNOWLEDGMENTS

We gratefully acknowledge the support from the U.S. Department of Energy, Office of Sciences, Office of Basic Energy Sciences to the SUNCAT Center for Interface Science and Catalysis. J.S.Y. gives special thanks to the U.S. Department of State for funding his studies through the International Fulbright Science & Technology Award program.

■ REFERENCES

(1) Dumesic, J. A.; Huber, G. W.; Boudart, M. In *Handbook of Heterogeneous Catalysis*, 2nd ed.; Ertl, G., Knözinger, H., Schüth, F., Weitkamp, J., Eds.; Wiley-VCH: Weinheim, Germany, 2008; pp 1−15.

(2) Koel, B. E.; Kim, J. In *Handbook of Heterogeneous Catalysis*, 2nd ed.; Ertl, G., Knözinger, H., Schüth, F., Weitkamp, J., Eds.; Wiley-VCH: Weinheim, Germany, 2008; pp 1593−1624.

(3) Hutchings, G. J. *Catal. Lett.* **2001**, *75*, 1−12.

(4) Rocha, T. C. R.; Hävecker, M.; Knop-Gericke, A.; Schlögl, R. *J. Catal.* **2014**, *312*, 12−16.

(5) Sachtler, W. M. H. In *Handbook of Heterogeneous Catalysis*, 2nd ed.; Ertl, G., Knözinger, H., Schüth, F., Weitkamp, J., Eds.; Wiley-VCH: Weinheim, Germany, 2008; pp 1585−1592.

(6) Studt, F.; Abild-Pedersen, F.; Bligaard, T.; Sørensen, R. Z.; Christensen, C. H.; Nørskov, J. K. *Science* **2008**, *320*, 1320−1322.

(7) Studt, F.; Sharafutdinov, I.; Abild-Pedersen, F.; Elkjær, C. F.; Hummelshøj, J. S.; Dahl, S.; Chorkendorff, I.; Nørskov, J. K. *Nat. Chem.* **2014**, *6*, 320−324.

(8) Andersson, M. P.; Bligaard, T.; Kustov, A.; Larsen, K. E.; Greeley, J.; Johannessen, T.; Christensen, C. H.; Nørskov, J. K.; Nørskov, J. K. *J. Catal.* **2006**, *239*, 501−506.

(9) Greeley, J.; Jaramillo, J. F.; Bonde, J.; Chorkendorff, I.; Nørskov, J. K. *Nat. Mater.* **2006**, *5*, 909−913.

(10) Hammer, B.; Nørskov, J. K. *Nature* **1995**, *376*, 238−240.

(11) Mavrikakis, M.; Hammer, B.; Nørskov, J. K. *Phys. Rev. Lett.* **1998**, *81*, 2819−2822.

(12) Daley, S. P.; Utz, A. L.; Trautman, T. R.; Ceyer, S. T. *J. Am. Chem. Soc.* **1994**, *116*, 6001−6002.

(13) Ludwig, W.; Savara, A.; Dostert, K.-H.; Schauermann, S. *J. Catal.* **2011**, *284*, 148−156.

(14) Wilde, M.; Fukutani, K.; Ludwig, W.; Brandt, B.; Fischer, J.-H.; Schauermann, S.; Freund, H.-J. *Angew. Chem., Int. Ed.* **2008**, *47*, 9289−9293.

(15) Xu, J.; Saeys, M. *J. Catal.* **2006**, *242*, 217−226.

(16) Xu, J.; Saeys, M. *J. Phys. Chem. C* **2009**, *113*, 4099−4106.

(17) Xu, J.; Chen, L.; Tan, K. F.; Borgna, A.; Saeys, M. *J. Catal.* **2009**, *261*, 158−165.

(18) Tan, K. F.; Chang, J.; Borgna, A.; Saeys, M. *J. Catal.* **2011**, *280*, 50−59.

(19) Jiang, K.; Xu, K.; Zou, S.; Cai, W.-B. *J. Am. Chem. Soc.* **2014**, *136*, 4861−4864.

(20) Chan, C. W. A.; Mahadi, A. H.; Li, M. M.-J.; Corbos, E. C.; Tang, C.; Jones, G.; Kuo, W. C. H.; Cookson, J.; Brown, C. M.; Bishop, P. T.; Tsang, S. C. E. *Nat. Commun.* **2014**, *5*, 5787−5793.

(21) Teschner, D.; Borsodi, J.; Wootsch, A.; Révay, Z.; Hävecker, M.; Knop-Gericke, A.; Jackson, S. D.; Schlögl, R. *Science* **2008**, *320*, 86−89.

(22) Grasemann, M.; Laurenczy, G. *Energy Environ. Sci.* **2012**, *5*, 8171−8181.

(23) Boddien, A.; Gärtner, F.; Federsel, C.; Sponholz, P.; Mellmann, D.; Jackstell, R.; Junge, H.; Beller, M. *Angew. Chem., Int. Ed.* **2011**, *50*, 6411−6414.

(24) Abild-Pedersen, F.; Greeley, J.; Studt, F.; Rossmeisl, J.; Munter, T. R.; Moses, P. G.; Skúlason, E.; Bligaard, T.; Nørskov, J. K. *Phys. Rev. Lett.* **2007**, *99*, 016105.

(25) Wang, S.; Petzold, V.; Tripkovic, V.; Kleis, J.; Howalt, J. G.; Skúlason, E.; Fernández, E. M.; Hvolbæk, B.; Jones, G.; Toftelund, A.; Falsig, H.; Björketun, M.; Studt, F.; Abild-Pedersen, F.; Rossmeisl, J.; Nørskov, J. K.; Bligaard, T. *Phys. Chem. Chem. Phys.* **2011**, *13*, 20760−20765.

(26) Yoo, J. S.; Abild-Pedersen, F.; Nørskov, J. K.; Studt, F. *ACS Catal.* **2014**, *4*, 1226−1233.

(27) Studt, F.; Abild-Pedersen, F.; Bligaard, T.; Sørensen, R. Z.; Christensen, C. H.; Nørskov, J. K. *Angew. Chem., Int. Ed.* **2008**, *47*, 9299−9302.

(28) Herron, J. A.; Scaranto, J.; Ferrin, P.; Li, S.; Mavrikakis, M. *ACS Catal.* **2014**, *4*, 4434−4445.

(29) Lausche, A. C.; Medford, A. J.; Khan, T. S.; Xu, Y.; Bligaard, T.; Abild-Pedersen, F.; Nørskov, J. K.; Studt, F. *J. Catal.* **2013**, *307*, 275−282.

(30) Grabow, L. C.; Hvolbæk, B.; Nørskov, J. K. *Top. Catal.* **2010**, *53*, 298−310.

(31) Tedsree, K.; Li, T.; Jones, S.; Chan, C. W. A.; Bagot, P. A. J.; Marquis, E. A.; Smith, G. D. W.; Yu, K. M. K.; Tsang, S. C. E. *Nat. Nanotechnol.* **2011**, *6*, 302−307.

(32) Zhang, S.; Metin, O.; Su, D.; Sun, S. *Angew. Chem., Int. Ed.* **2013**, *52*, 3681−3684.

(33) Cho, J.; Lee, S.; Han, J.; Yoon, S. P.; Nam, S. W.; Choi, S. H.; Lee, K.-W.; Ham, H. C. *J. Phys. Chem. C* **2014**, *118*, 22553.

(34) Huang, Y.; Zhou, X.; Yin, M.; Liu, C.; Xing, W. *Chem. Mater.* **2010**, *22*, 5122−5128.

(35) Zhou, X.; Huang, Y.; Xing, W.; Liu, C.; Liao, J.; Lu, T. *Chem. Commun.* **2008**, *30*, 3540−3542.

(36) Medford, A. J.; Wellendorff, J.; Vojvodic, A.; Studt, F.; Abild-Pedersen, F.; Jacobsen, K. W.; Bligaard, T.; Nørskov, J. K. *Science* **2014**, *345*, 197−200.

(37) Bahn, S. R.; Jacobsen, K. W. *Comput. Sci. Eng.* **2002**, *4*, 56−66.

(38) Giannozzi, P.; Baroni, S.; Bonini, N.; Calandra, M.; Car, R.; Cavazzoni, C.; Ceresoli, D.; Chiarotti, G. L.; Cococcioni, M.; Dabo, I.; Dal Corso, A.; Fabris, S.; Fratesi, G.; de Gironcoli, S.; Gebauer, R.; Gerstmann, U.; Gougoussis, C.; Kokalj, A.; Lazzeri, M.; Martin-Samos, L.; Marzari, N.; Mauri, F.; Mazzarello, R.; Paolini, S.; Pasquarello, A.; Paulatto, L.; Sbraccia, C.; Scandolo, S.; Sclauzero, G.; Seitsonen, A. P.; Smogunov, A.; Umari, P.; Wentzcovitch, R. M. *J. Phys.: Condens. Matter* **2009**, *21*, 395502.

(39) Wellendorff, J.; Lundgaard, K. T.; Møgelhøj, A.; Petzold, V.; Landis, D. D.; Nørskov, J. K.; Bligaard, T.; Jacobsen, K. W. *Phys. Rev. B: Condens. Matter Mater. Phys.* **2012**, *85*, 235149.

DOI: 10.1021/acscatal.5b01497
ACS Catal. 2015, 5, 6579−6586

(40) Wellendorff, J.; Silbaugh, T. L.; Garcia-Pintos, D.; Nørskov, J. K.; Bligaard, T.; Studt, F.; Campbell, C. T. *Surf. Sci.* **2015**, *640*, 36−44.
(41) Studt, F.; Abild-Pedersen, F.; Varley, J. B.; Nørskov, J. K. *Catal. Lett.* **2013**, *143*, 71−73.
(42) Studt, F.; Behrens, M.; Kunkes, E. L.; Thomas, N.; Zander, S.; Tarasov, A.; Schumann, J.; Frei, E.; Varley, J. B.; Abild-Pedersen, F.; Nørskov, J. K.; Schlögl, R. *ChemCatChem* **2015**, *7*, 1105−1111.
(43) Laasonen, K.; Car, R.; Lee, C.; Vanderbilt, D. *Phys. Rev. B: Condens. Matter Mater. Phys.* **1991**, *43*, 6796−6799.
(44) Monkhorst, H. J.; Pack, J. D. *Phys. Rev. B* **1976**, *13*, 5188−5192.
(45) Henkelman, G.; Uberuaga, B. P.; Jónsson, H. *J. Chem. Phys.* **2000**, *113*, 9901−9904.
(46) Peterson, A. A.; Abild-Pedersen, F.; Studt, F.; Rossmeisl, J.; Nørskov, J. K. *Energy Environ. Sci.* **2010**, *3*, 1311−1315.
(47) Chuang, F. C.; Ciobanu, C. V.; Shenoy, V. B.; Wang, C. Z.; Ho, K. M. *Surf. Sci.* **2004**, *573*, L375−L381.
(48) Sierka, M. *Prog. Surf. Sci.* **2010**, *85*, 398−434.
(49) Johnston, R. L. *Dalton Trans.* **2003**, *22*, 4193−4207.

DOI: 10.1021/acscatal.5b01497
ACS Catal. 2015, 5, 6579−6586